



Molecular dynamics simulation on flow boiling heat transfer characteristics

Shanshan Miao, Guodong Xia^{*}, Ran Li

College of Mechanical and Energy Engineering, Beijing University of Technology, Beijing 100124, China

ARTICLE INFO

Keywords:

Flow boiling
Driving force
Heat transfer
Molecular dynamics

ABSTRACT

In this paper, a flow boiling model consisting of an argon liquid and a copper solid wall has been developed using a molecular dynamics method to understand the effects of driving force and substrate temperature on the flow boiling characteristics at the nanoscale. The variation of parameters such as the morphology of liquid argon, the near-wall liquid temperature and heat flux are analyzed for different driving forces and substrate temperatures. The results show that the boiling onset time at lower substrate temperatures is mainly determined by the driving force, and the boiling onset time is gradually delayed as the driving force increases. The main mechanism is nucleation boiling, and the heat flux in the stabilization stage decreases with increasing driving force. In contrast, the boiling onset time at higher substrate temperatures is determined by both the substrate temperature and the driving force. At higher substrate temperature and lower driving force, atoms near the substrate are more likely to gain energy to break away from the surface, and therefore film boiling occurs, which produces a vapor film near the substrate during heating, leading to deterioration of heat transfer and a decrease in the average heat flux instead.

1. Introduction

In recent years, with the rapid advancement of science and technology, various breakthroughs have been made in the field of electronics, and electronic devices are gradually developing towards miniaturization and high-power. Flow boiling within microchannel heat sinks has become a research hotspot in the field of the microelectronic heat dissipation due to its high integration and superior heat transfer ability [1–4]. The characteristics of fluid flow and heat transfer at the microscale are significantly different from those at conventional scale [5], which leads to problems at the micro/nano scale. The interface effect has a more significant impact on flow at the nanoscale, where the continuity assumption is not valid and traditional simulation as well as experimental methods are subject to numerous limitations. In this context, molecular dynamics (MD) methods focusing on microscopic particles such as molecules, atoms, or ions have become an important tool for studying micro and nano scale boiling processes [6–8].

The microscopic mechanism of the pool boiling has been investigated by molecular dynamics [9–11]. Deng et al. [12] found that heat transfer could be maximally enhanced by the combination of hydrophilic and hydrophobic walls. Additionally, different hydrophilic and hydrophobic patterns could lead to different heat transfer performance. Therefore, the shape of the bubbles, the nucleation temperature, and the

rate of nucleation of the bubbles could be controlled by the design of hydrophilic and hydrophobic patterns. Zhou et al. [13] explored the mechanism of enhanced heat transfer on rectangular groove surfaces. The results showed that heat accumulation grows with increasing cavity depth, but the increasing effect slows down with a further increase in cavity depth. Therefore, there was an optimal cavity depth that could maximally enhance nucleate boiling. Wang et al. [14] compared the boiling process on solid copper and liquid metal grafted surfaces. It was found that heat transfer on the liquid metal surface was more efficient in improving the boiling heat transfer capability.

The microscopic mechanism of convective heat transfer in graphene nano-channels was investigated by Marable et al. [15] They introduced a “heat pump model” that divides the fluid region into a forcing region, a temperature reset region, and a free development region. Chakraborty et al. [16–18] investigated the effect of surface structure on heat transfer in single-phase flow using the thermal pump model and found that rough nanochannels significantly enhanced heat convection. The overall heat transfer rate was better compared to smooth nanochannels, regardless of the nanostructure morphologies.

Amirhosein et al. [19] explored the effect of spherical surface structure on flow boiling by simulating annular flow, in which two liquids in the form of thin films covered the walls of the channel, and the central area was set as a vapor region. The results showed that although

^{*} Corresponding author.

E-mail address: xgd@bjut.edu.cn (G. Xia).

the rough spherical geometry of the surfaces was not conducive to trapping atoms, the boiling process was enhanced. Xu et al. [20] explored the effect of cone, cubic and spherical surfaces on annular flow boiling and found that argon atoms appeared earlier at the center of microchannels with cubic barriers. Rostami et al. [21] observed the flow velocity was observed to decrease due to the cube barrier, and the external force was increased from 0.002 eV/Å to 0.02 eV/Å, leading to turbulence in the microchannel and unstable atomic distribution. Yin et al. [22] investigated the effect of driving force and substrate temperature on the heat transfer characteristics of nanofluid flow during boiling process and found that both flow velocity and substrate temperature have a large effect on the heat transfer process at lower substrate temperature, but as the heating temperature increased, the impact of flow velocity on heat transfer performance diminished.

Although there have been many studies on two-phase heat transfer using MD, most of the studies have primarily focused on pool boiling; and the limited flow boiling studies applied a uniform driving force on all atoms in horizontal direction, neglecting the influence of the inlet cold fluid which is actually crucial for the flow boiling process, especially at the nanoscale. Therefore, in this work, the flow process is simulated using the “heat pump model”, and the boiling heat transfer of liquid argon on a copper substrate is systematically investigated by molecular dynamics. The effects of driving force and substrate temperature on the boiling conditions are investigated, and the mechanism for enhancing the boiling heat transfer is explored.

2. Simulation method and process

2.1. Simulation system

As shown in Fig. 1(a), the dimensions of the simulated system are 37 nm (x) × 3.25 nm (y) × 18 nm (z). The working fluid uses argon (Ar) atoms because argon is monoatomic and only van der Waals forces need to be considered between the atoms. The fluid domain contains both liquid argon and vapor argon that undergo flow and heat transfer processes. Copper is widely used in the field of heat transfer due to its good thermal conductivity [23–25], therefore copper atoms are chosen for the

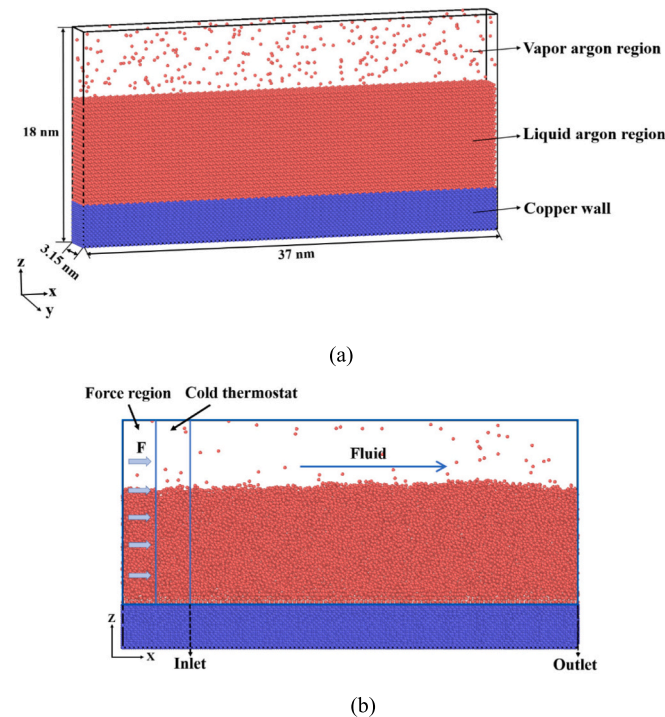


Fig. 1. Schematic diagram of the simulation domain.

solid wall surfaces. Liquid Ar atoms with a thickness of 9 nm are arranged above the copper surface. A vapor region is created by randomly dispersing 300 Ar atoms between the liquid Ar and the upper surface to provide a vapor layer at the initial moment. Liquid argon exhibits a face-centered cubic (FCC) lattice structure at the initial moment, with a lattice constant of 0.58 nm and a density of 1.367 g/cm³. The local magnified view of Fig. 1 shows that the argon vapor region is sparsely distributing argon atoms, which are widely spaced. The atoms in the argon liquid region are almost closely adjacent to each other, but irregularly distributed. The copper atoms are arrayed in an FCC with a lattice constant of 0.361 nm. The outermost two layers of copper atoms remain fixed to prevent system collapse and the middle three layers are temperature controlled by applying a Langevin thermostat to maintain a fixed substrate temperature. In addition, nine layers of copper atoms adjacent to the working fluid act as thermal conductive layers, facilitating heat transfer between the higher temperature walls and the working fluid. The constant of harmonic spring force is 2.93 eV/Å², so that the solid atoms can only vibrate around their origin position. The local magnified view shows that the copper atoms are arranged in a very regular pattern. Periodic boundary conditions are employed in the x and y directions to simulate infinite system size, while fixed boundary conditions are applied in the z direction to mimic confined flow within the simulated system. The reflective wall surface on the upper wall prevents momentum and energy exchange between the wall and the Ar atoms, achieving no-shear and adiabatic conditions.

Considering the challenges posed by maintaining a constant inlet temperature and ensuring energy conservation in the actual process, the heat pump model is used and the fluid domain is divided into three distinct regions along the flow direction: a force region at 0 < x < 10.0 Å, a temperature reset region at 10.0 Å < x < 17.0 Å, and a free development region at 17.0 Å < x < 370.0 Å (Fig. 1(b)). Firstly, a driving force F in the positive direction along the x-axis is applied to all the atoms passing through the force region to provide the driving force for the liquid flow. Subsequent temperature correction of the atoms, and the Langevin thermostat is employed to reset the temperature exclusively for the fluid atoms residing within the temperature reset region. By resetting the temperature, a uniform flow with a consistent inlet temperature condition can be established and the convective heat transfer process in the microchannel can be explored in the range 17.0 Å < x < 370 Å. Fluid enters the channel from the inlet at the specified initial temperature of 86 K. The flow of liquid argon is sustained by imposing a constant driving force along the x-direction on all fluid atoms traversing the forcing region (0–10.0 Å).

2.2. Potential models and procedure

The Lennard-Jones (LJ) potential functions are used for the Cu-Cu and Ar-Ar interactions during the simulation, with the following expression:

$$U_{ij}(r_{ij}) = 4\epsilon \left[\left(\frac{\sigma}{r_{ij}} \right)^{12} - \left(\frac{\sigma}{r_{ij}} \right)^6 \right] \quad (1)$$

where ϵ and σ are the energy and length parameters, and r_{ij} is the distance between molecule i and molecule j. For the Cu-Cu interaction, the energy and length parameters are taken as $\epsilon_{\text{Cu-Cu}} = 0.40933$ eV and $\sigma_{\text{Cu-Cu}} = 0.2338$ nm, respectively. For the Ar-Ar interaction, the energy and length parameters are taken as $\epsilon_{\text{Ar-Ar}} = 0.01033$ eV and $\sigma_{\text{Ar-Ar}} = 0.3405$ nm, respectively. The cutoff radius is set to $3.5\sigma_{\text{Ar-Ar}}$, i.e., 1.2 nm.

The interaction between Cu and Ar atoms can be illustrated by the modified form of the L-J potential [26]:

$$U_{ij}(r_{ij}) = 4\epsilon_{\text{sl}} \left[\left(\frac{\sigma_{\text{sl}}}{r_{ij}} \right)^{12} - \beta \left(\frac{\sigma_{\text{sl}}}{r_{ij}} \right)^6 \right] \quad (2)$$

$$\sigma_{sl} = \frac{1}{2}(\sigma_s + \sigma_l) \quad (3)$$

$$\varepsilon_{sl} = \alpha \sqrt{\varepsilon_s \varepsilon_l} \quad (4)$$

where the subscripts s and l represent solids and liquids, respectively. Typically, the coefficient β is set to 1. The solid-liquid interaction intensity, i.e., the interfacial wettability, can be adjusted by changing the energy coefficient α in the current study. We simply took a constant α (0.4) since the effect of wall wettability is out of the present scope. Our previous work showed that $\alpha = 0.4$ is the hydrophilic surface [27]. In this way, eqs. (2–4) follow the conventional Lorentz-Berthelot principle [28].

In the simulation, the computational region is equally divided into layers along the z-axis, and then the temperature in each layers is calculated, where the fluid temperature of the i -th layers is calculated as

$$T_i = \sum_{j=1}^{N_i} m v_j^2 / 3N_i k \quad (5)$$

where m is the mass of the fluid molecule, v_j is the velocity of the j -th fluid molecule in the i -th bin; N_i is the total number of atoms in the i -th layers; k is the Boltzmann constant.

The time step is set to 2 fs. Initially the system performs an equilibrium simulation using a Langevin thermostat in the canonical ensemble (NVT, i.e., constant atom number, volume and temperature) with an equilibrium temperature of 86 K for 4 ns. Then, the solid wall is

then elevated to the target temperature by running 100,000 steps which is 0.2 ns in a microcanonical ensemble (NVE) ensemble. Finally, an 4 ns data collection phase is executed in the NVE to study the bubble nucleation and growth process. Both the second and third phases are non-equilibrium phases, and the start of the second phase is defined as 0 ps unless otherwise noted. This study is implemented using the open-source molecular dynamics simulation software LAMMPS and the atomic trajectory is visualized by OVITO software [29].

3. Results and discussion

3.1. Effect of substrate temperature and driving force on bubble dynamics behavior

The boiling initial temperature is an important parameter of the boiling process and is defined as the lowest substrate temperature that can nucleate bubbles within 8 ns after the substrate temperature is raised to the target value. Calculation accuracy is 1 K. The results show that the boiling initial temperature is 178 K, 184 K and 186 K at $F = 200$ fN, $F = 300$ fN and $F = 400$ fN, respectively. The boiling initial temperature increases with increasing driving force. To observe the phenomena of evaporation, boiling and intense boiling at the same time, the following three cases with substrate temperatures of 180 K, 190 K and 200 K are investigated.

The flow is induced by subjecting the Ar atoms in the forcing region to driving forces in the x-direction of $F = 200$ fN, 300 fN and 400 fN ($1 \text{ fN} = 10^{-15} \text{ N}$), respectively. To investigate the flow velocity

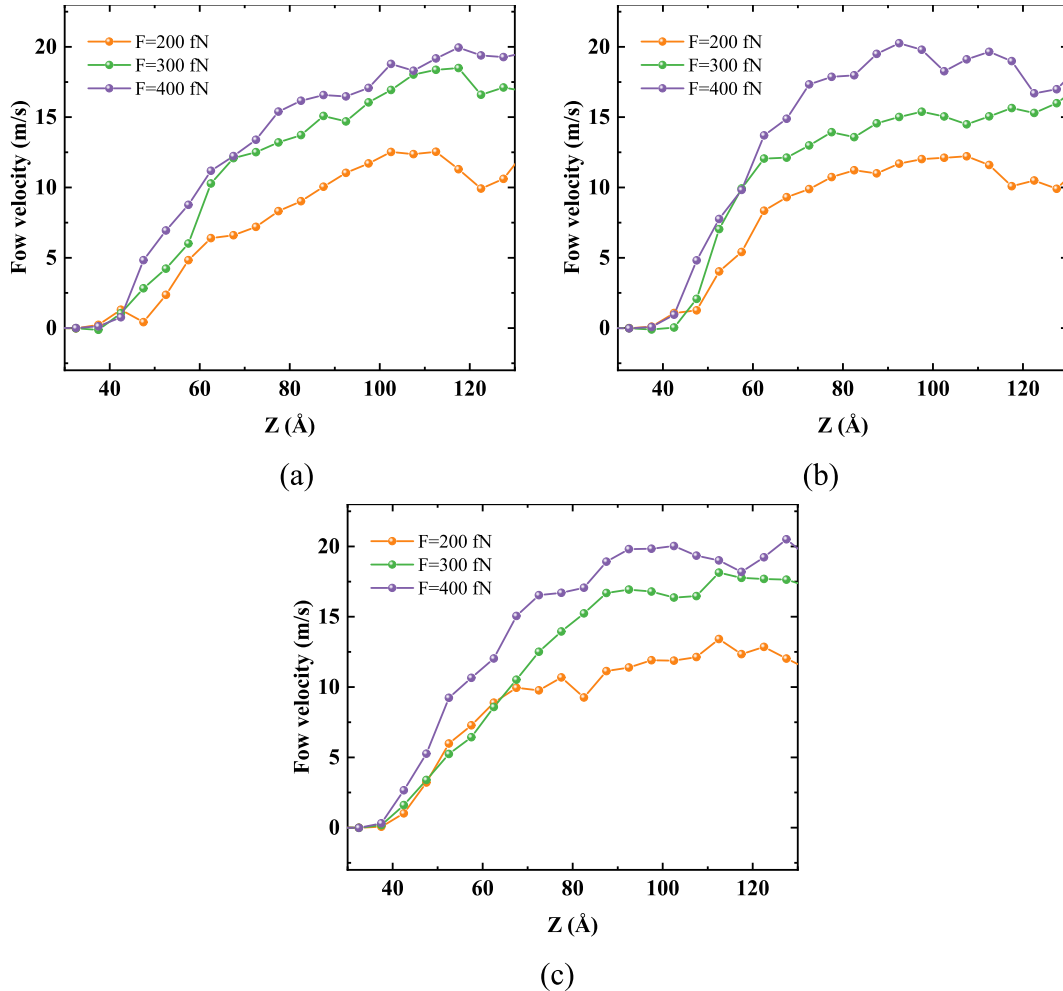


Fig. 2. Variation of flow velocity of liquid along z-direction under different forces during the first 500 ps (a) $T_w = 180$ K, (b) $T_w = 190$ K, (c) $T_w = 200$ K.

distributions under different driving forces and explore their effect on the boiling process, the systems is discretized into 35 cells along the z-direction, and the height of each cell is 5 Å. The average flow velocity distribution along the z-direction for different driving forces during the first 500 ps is shown in Fig. 2. As there is an attraction of the solid wall to the liquid atoms, it can be seen that there is a significant velocity gradient in the liquid region and it increases with the magnitude of driving force. The minimum flow velocity near the wall is close to 0 m/s, while the overall flow velocity ranges from 0 m/s to 20 m/s. The average flow velocity at a fixed driving force slightly increases with the temperature (Fig. 3), and this can be attributed to the easier generation of small voids within the fluid at higher temperatures, which leads to a decrease in the interaction force between the fluid atoms and the solid atoms, thereby increasing the average flow velocity of liquid. However, the effect of wall temperature on the average flow velocity of liquid decreases with increasing driving force, and the average flow velocity is the same for wall temperatures of 190 K and 200 K at $F = 400$ fN.

At macroscopic scale, the complete process of bubble nucleation, growth and detachment can be observed. At nanoscale however, the limited thickness of the liquid film only allows nucleation and growth to be visible, and the bubble detachment cannot be traced [30]. Snapshots of the bubble nucleation process in the channel at different temperatures are shown in Fig. 4 to Fig. 6. At the early stage of heating, liquid Ar atoms absorb energy from the Cu surface and undergo evaporation, resulting in the formation of numerous tiny voids in the liquid region near the Cu surface, which coalesce to nucleate and develop into larger bubbles. At a wall temperature of 180 K, the temperature reset region in the inlet section could affect the overall heat transfer and flow pattern. As shown in Fig. 4(a), at $F = 200$ fN, a bubble nucleus begins to be produced at 2100 ps, and the bubble grows while moving to the right under the driving force, moving to the channel outlet at 2440 ps. Further increasing the driving force, as shown in Fig. 4(b) and Fig. 4(c), no bubbles are generated within 8000 ps, and single-phase flow is dominant.

When the wall temperature rises to 190 K, the bubbles nucleate and continue to grow. Although the temperature reset region affects the growth of bubbles, it is not sufficient to make the bubbles extinguish. It can be seen from Fig. 5 that the vapor phase exists in the form of single bubble, which gradually grows upwards and sideways with heating time and moves towards the outlet of the channel. The volume of the bubble slightly decreases when it moves near the outlet due to the periodic image of the inlet temperature reset region. Ultimately, there is no vapor film formed on the wall surface at this heat temperature.

As the wall temperature continues to increase, it can be observed that when the wall temperature reaches 200 K, liquid argon first absorbs heat

to form the bubble. At $F = 200$ fN, as illustrated in Fig. 6(a), multiple bubble nuclei are generated at high temperatures, unlike in Fig. 4(a) where only one bubble nucleus is shown. This is partly since the higher temperature heat source can provide more activation energy and therefore more likely to produce bubble nuclei. On the other hand, it is due to the more active motion of fluid molecules, enhanced thermal motion, and increased mutual collisions between atoms, resulting in the simultaneous appearance of multiple nucleation sites. The volume of the bubble gradually increases with further heating, forming a vapor film near the wall. The vapor film causes the argon atoms near the solid surface to lift from the surface, resulting in the complete coverage of the wall by the vapor film, which represents the onset of film boiling. It is difficult to transfer energy from solid atoms to liquid argon atoms during film boiling, leading to deterioration of heat transfer. It is worth noting that beneath the vapor film there is still a thin layer of liquid atoms attached on the Cu wall. These atoms are adhered to Cu atoms by the strong solid-liquid interaction and are non-evaporative, hence contributed to no heat transfer [31]. Increasing the driving force further, a bubble nucleus can form in the channel, but no film boiling occurs.

There exists a boiling onset time in flow boiling at the nanoscale, which is the critical point for the transition of the working fluid from single-phase to two-phase and represents the beginning of nucleate boiling. Boiling onset time is an important parameter and has been widely evaluated for the performance of flow boiling. In this study, the onset of boiling is defined as the moment when the volume of the vapor phase reaches $40,000 \text{ Å}^3$. The boiling onset times in the flat-walled channel under different driving forces are shown in Table 1. Generally, higher wall temperatures enable the liquid to absorb more heat, leading to earlier boiling. Therefore, the onset time of boiling shortened with the increase of wall temperature under the same driving force. From the energy perspective, higher wall temperatures result in a faster rate of change of liquid energy, then it becomes easier to break the energy barrier to promote the nucleation of bubble, which is consistent with the previous snapshots in Fig. 4. When the wall temperature is low ($T_W = 180$ K), the increase in driving force leads to more Ar atoms passing through the cold thermostat per unit of time, which equates to more influx of low-temperature fluid into the channel, thus increasing heat dissipation. This in turn prevents bubble nucleation. On the other hand, the motion of atoms destabilizes the void's stability, inhibiting its aggregation into a bubble nucleus, and hence the onset of boiling time increases with the increase in driving force. Thus, bubbles nucleate at 2100 ps when $F = 200$ fN. Increasing the driving force further, boiling no longer occurs. When $T_W = 190$ K, the onset of boiling time increases with increasing driving force. Further increase in substrate temperature ($T_W = 200$ K), the heat transfer capacity from the wall to the fluid rises sharply enabling a quicker response to boiling. Consequently, the onset of boiling at high temperatures depends more on the heating temperature than on the driving force [22]. Lower boiling onset times suggest a higher likelihood of nuclear state boiling, which is beneficial in engineering practice.

The volume of bubble is further calculated in order to quantitatively describe and analyses the nucleation and growth process of the bubble. First, the fluid domain is divided into cells of length and width 5 Å, respectively. The threshold value is set as half of the sum of the dimensionless number densities of the liquid and vapor phase. When the dimensionless number density within a cell falls below this threshold value, it is classified as the vapor phase. The curves of vapor phase volume with time at different driving force are shown in Fig. 7. Defining the time of nucleation when the volume of the vapor reaches $40,000 \text{ Å}^3$ is marked with a red straight line in Fig. 7. At a wall temperature of 180 K, as shown in Fig. 7(a), the bubble is able to nucleate only at $F = 200$ fN. Nucleation conditions are first reached around 2100 ps, and the volume of the vapor phase grows rapidly to reach a peak. Thereafter, the bubble moves to the outlet of the channel, where the volume of the vapor phase gradually decreases under the influence of the inlet cold thermostat region. Bubble is completely eliminated at around 3400 ps. Heating is

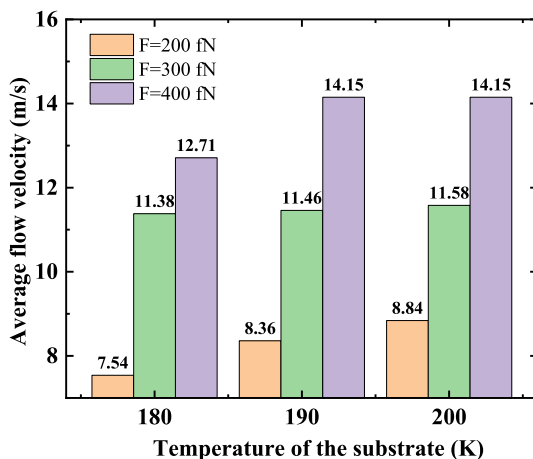


Fig. 3. Variation of average flow velocity of liquid under different forces during the first 500 ps.

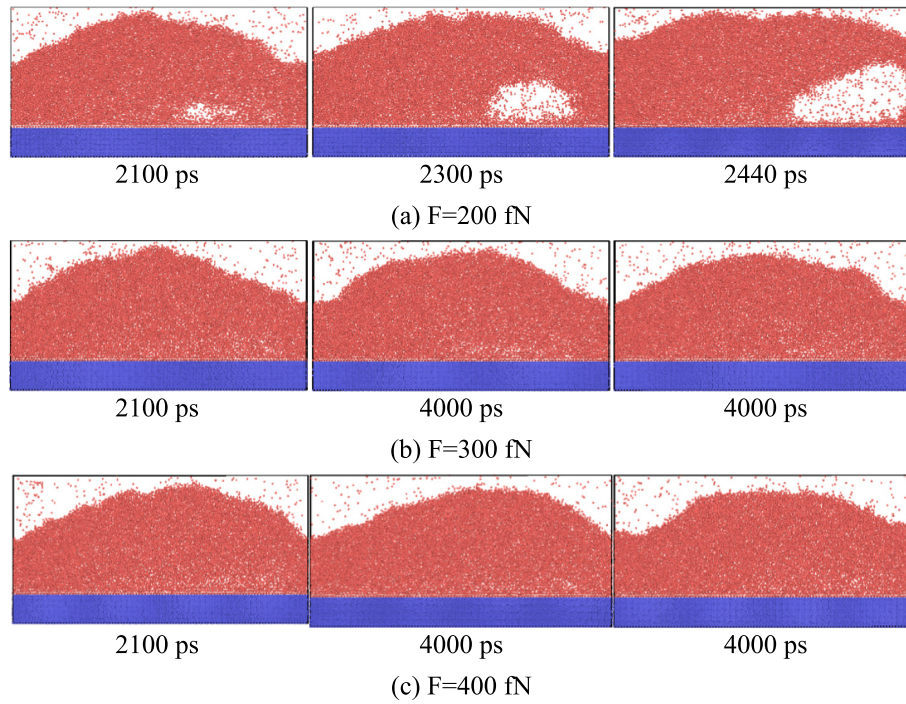


Fig. 4. Snapshot of the nucleation boiling process at a substrate temperature of 180 K (a) $F = 200$ fN, (b) $F = 300$ fN, (c) $F = 400$ fN.

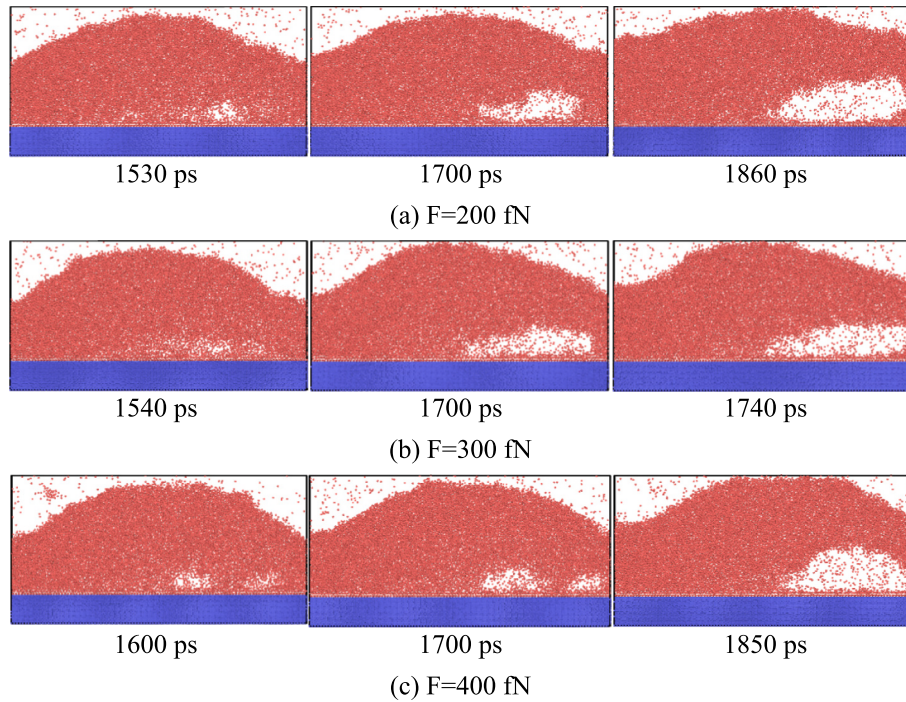


Fig. 5. Snapshot of the nucleation boiling process at a substrate temperature of 190 K (a) $F = 200$ fN, (b) $F = 300$ fN, (c) $F = 400$ fN.

continued until bubble formation occurs again at 6500 ps, and the volume of the vapor phase reaches a second peak at about 7000 ps and then decreases. Increasing the driving force further, it can be seen that the vapor volume is always below $40,000 \text{ \AA}^3$, which means that no boiling occurs at $F = 300$ fN and $F = 400$ fN. Increasing the wall temperature to 190 K, the vapor volume is in an oscillatory state for all three driving forces as shown in Fig. 7(b). Further increasing the wall temperature to 200 K, as shown in Fig. 7(c), the vapor volume exhibits rapid growth after the formation of bubble nucleation [32]. The vapor volume all

oscillate at a higher level, especially when $F = 200$ fN, the vapor volume is always at the highest position.

In order to further investigate some details of the flow boiling process, the change in the center of mass height of the fluid along the z-axis direction is monitored, using the solid-liquid interface as the reference point, and the results are shown in Fig. 8(a). Comparing the results in Fig. 7 and Fig. 8(a), it is interesting to find that at the very early stage (0–1000 ps), the fluid center of mass has ascended while the vapor phase volume still remains at zero. The center of mass height stays stable for

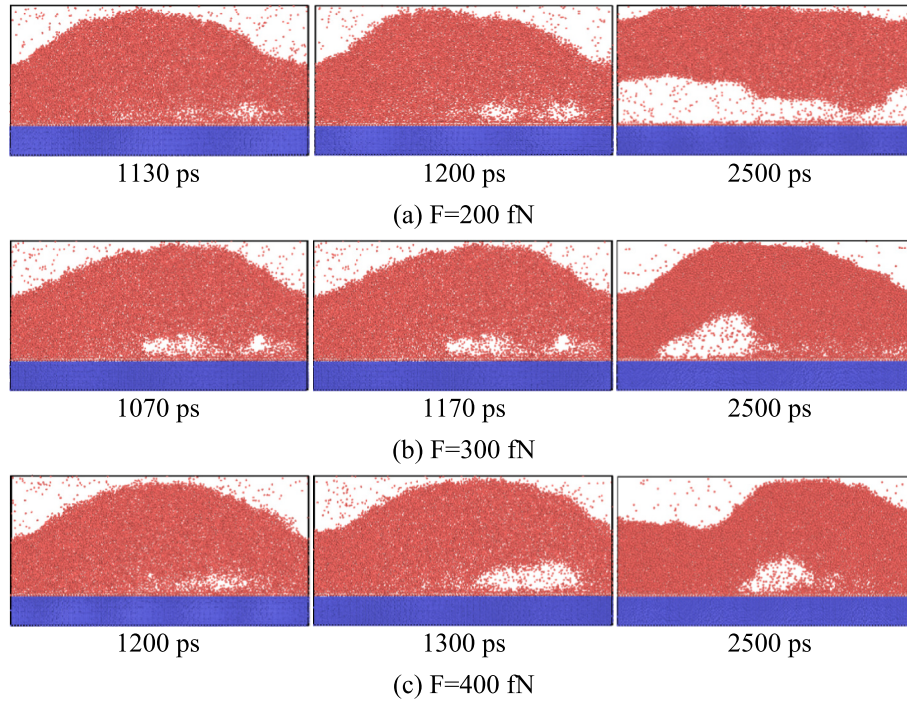


Fig. 6. Snapshot of the nucleation boiling process at a substrate temperature of 200 K (a) $F = 200$ fN, (b) $F = 300$ fN, (c) $F = 400$ fN.

Table 1

Onset of boiling time (ps).

Temperature Driving force	$T_W = 180$ K	$T_W = 190$ K	$T_W = 200$ K
$F = 200$ fN	2100	1530	1130
$F = 300$ fN	–	1540	1070
$F = 400$ fN	–	1600	1200

some time near the nucleation time and then rises rapidly again. The greater the driving force at the same wall temperature the longer the center of mass is highly stable during nucleation, this is because the greater the driving force the more difficult it is to accumulate energy near the wall. This finding demonstrates that whether nucleation occurs, there exist numerous small voids within the liquid region, and as the walls continue to heat the small voids continue to grow and coalesce into bubbles that are defined by the sum of the interconnected voids [31]. As shown in the partial enlargement of Fig. 8(b), before bubble nucleation (0–1000 ps) the liquid center of mass height growth rate increases with the increase of driving force. However, after nucleation instead the liquid center of mass height growth rate is maximum at $F = 200$ fN, when the wall temperature is 190 K and 200 K. This phenomenon may be attributed to the increased intensity of atom collisions with increasing driving force, resulting in a higher probability of small void formation. However, at the same time with increasing driving force more cold fluid enters into the channel through the temperature reset region, which slows down the growth of bubbles, and thus the rate of growth of bubbles decreases with the increase of driving force after nucleation.

The liquid near the wall is the key to the transfer of energy from the solid wall to the liquid. Thus, the liquid region at a height of 20 Å near the wall (35 Å to 55 Å) is defined as the nucleation region, and the change in the liquid atomic density in this region with heating time is observed. From Fig. 9, we can observe that the density of the liquid at the beginning of heating is slightly higher than 1.367 g/cm³, which is caused by atoms adsorbed near the substrate. Nucleation of bubble at atomic density of 0.98 g/cm³. It can be seen that at temperatures of 180 K, the atomic density in the nucleation region first decreases rapidly and then stabilizes around a higher value. Only when $F = 200$ fN there is a

period of time in between when the density of atoms is less, which indicates that a large number of atoms leave the nucleation region, which implies the nucleation and growth of bubbles. After a certain level of bubble growth, the heat absorbed by the liquid argon from the substrate reaches roughly the same amount of cold entering the channel inlet, which is not enough to support the development of bubbles towards the vapor film. When the substrate temperature is 200 K, the substrate can provide more heat to the liquid argon, and more liquid argon atoms get energy to break the energy potential barrier and thus detach from the substrate. Thus, the atomic density at a low value as heating proceeds.

3.2. Effect of substrate temperature and driving force on fluid temperature and heat flux

In order to fully understand the effect of substrate temperature and driving force on flow boiling and to reveal its potential mechanism of enhanced heat transfer, fluid temperature and heat flux are examined and analyzed. The liquid in close proximity to the solid wall plays a crucial role in energy transfer and changes in the boiling state. Fig. 10 shows the temperature change of the liquid in the nucleation region at different wall temperatures. It can be seen that the trend of temperature change is the same, in the initial stage, the liquid has been absorbing heat and accumulating energy for the nucleation of bubbles, and the temperature rises sharply. As the temperature difference between the liquid and the solid wall decreases, the liquid temperature starts to increase slowly around 1000 ps. The liquid temperature trend is the same for the different driving forces, with no significant differences. Fig. 11 gives the variation of the average temperature during the steady stage (1000 ps ~2000 ps). It can be seen that the average temperature increases as the wall temperature increases. For the same wall temperature, the average temperature decreases with the increase of driving force, which indicates that better heat transfer can be achieved at $F = 200$ fN.

The heat flux through the system can be calculated by the following equation:

$$q = \frac{1}{A} \frac{\Delta E_{Ar}}{\Delta t} \quad (6)$$

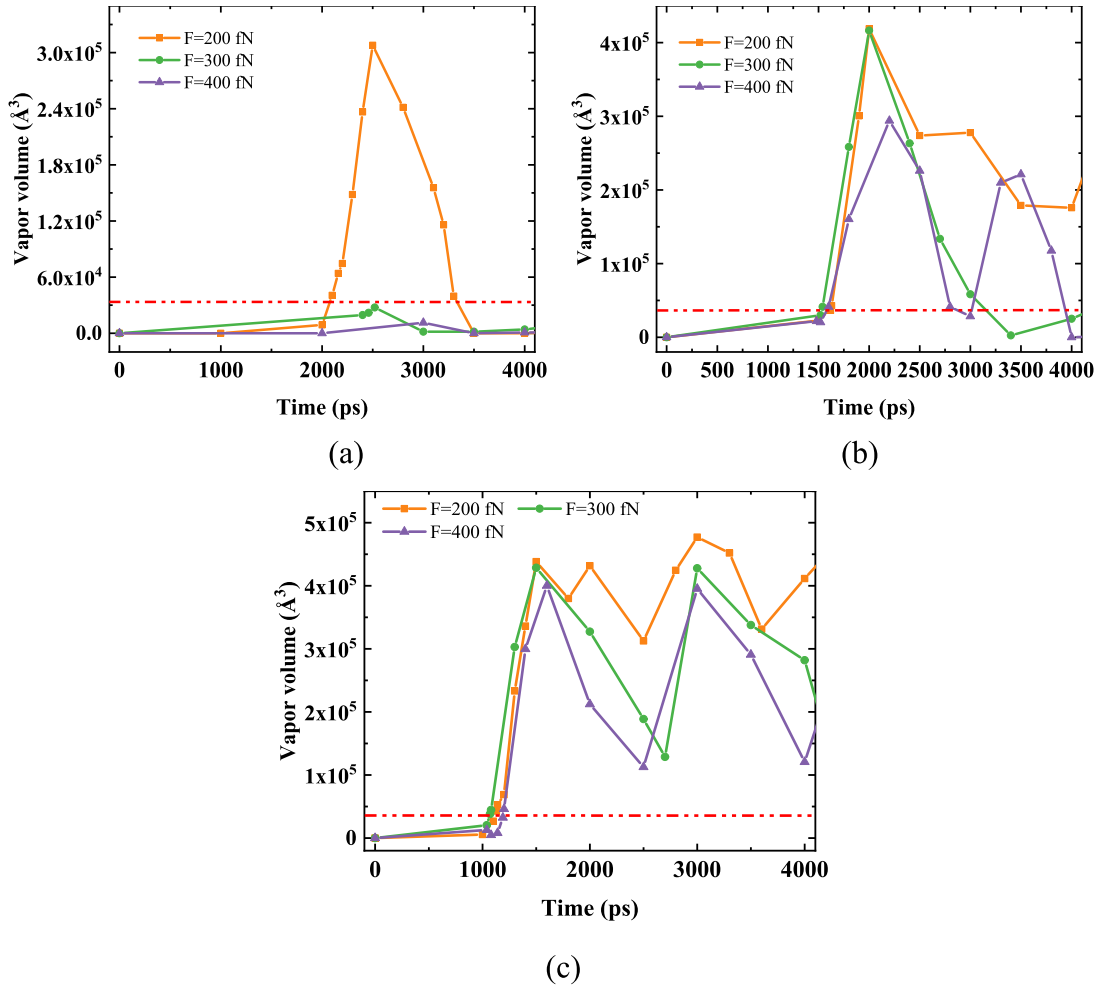


Fig. 7. The change of vapor volume with time under different driving forces (a) $T_W = 180$ K, (b) $T_W = 190$ K, (c) $T_W = 200$ K.

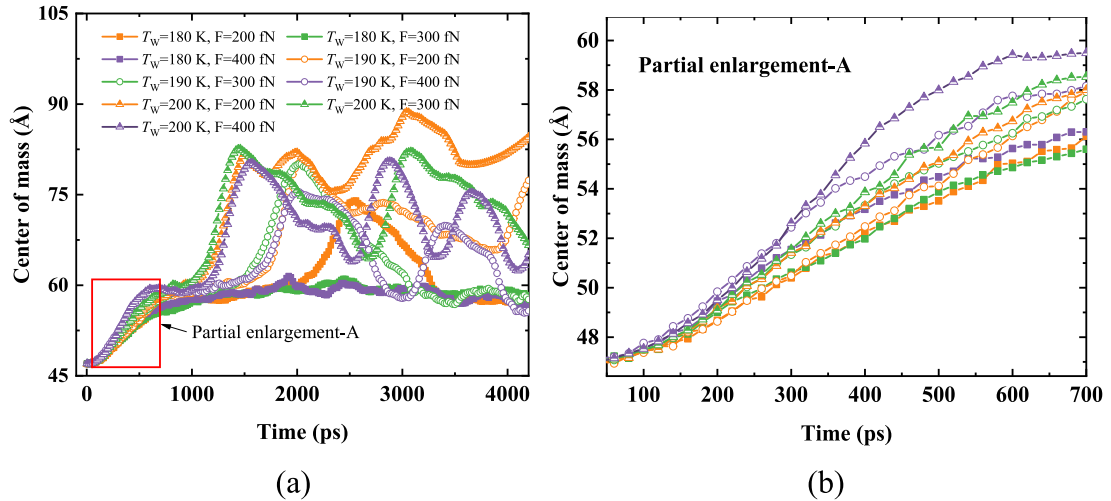


Fig. 8. Variation of liquid center of mass with time under different driving forces.

where ΔE_{Ar} is the total energy change of argon atoms, Δt is the time step, and A is the area of the heating surface.

The heat transfer efficiency can be evaluated by the heat flux to further quantify the effect of substrate temperature and driving force on the heat transfer performance. Fig. 12 shows the variation of heat flux with time for different driving forces. The curves are smoothed using the

origin software for ease of observation. The maximum heat flux occurs approximately at the beginning of the third stage. At lower temperatures ($T_W = 180$ K and $T_W = 190$ K), the maximum heat flux decreases with increasing driving force for the same temperature, and the maximum heat flux increases with increasing temperature for the same driving force. When $T_W = 200$ K, the maximum heat flux is greatest at $F = 300$

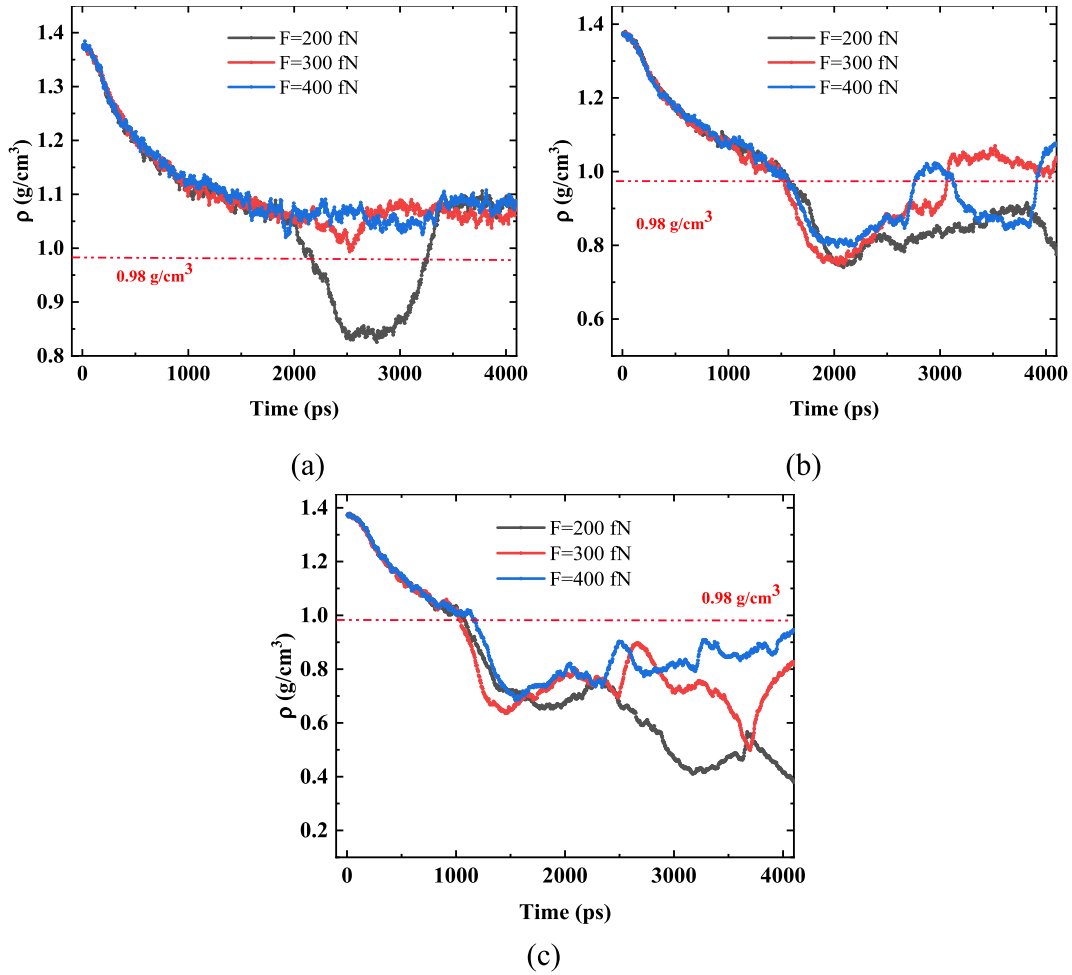


Fig. 9. Variation of argon density in the nucleation region with time (a) $T_W = 180$ K, (b) $T_W = 190$ K, (c) $T_W = 200$ K.

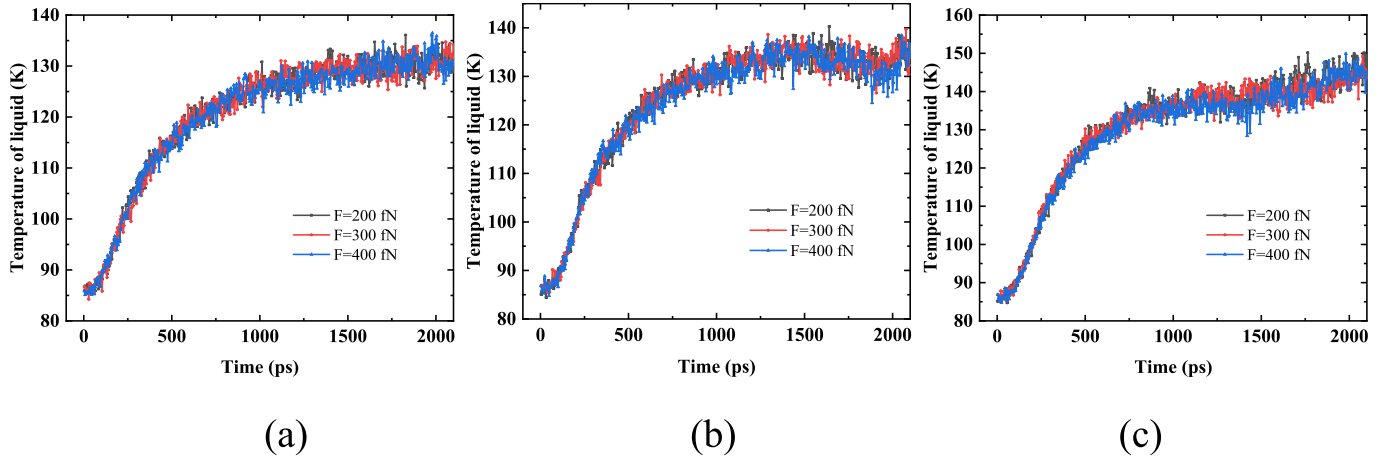


Fig. 10. Variation of liquid temperature with time in the nucleation region (a) $T_W = 180$ K, (b) $T_W = 190$ K, (c) $T_W = 200$ K.

fN.

The heat flux begins to stabilize after 2000 ps, and the average heat flux during the stabilization stage (2000 ps \sim 4000 ps) is shown in Fig. 13. At lower temperatures ($T_W = 180$ K and $T_W = 190$ K), the average heat flux decreases with increasing driving force for the same temperature. At $T_W = 180$ K, the average heat flux at $F = 200$ fN increased by 26 times compared to $F = 400$ fN. At $T_W = 190$ K, the average heat flux at $F = 200$ fN increased by 102 times compared to $F =$

400 fN. When $T_W = 200$ K, the average heat flux increases with increasing driving force. At $T_W = 200$ K, the average heat flux at $F = 400$ fN increased by 11.2 times compared to $F = 200$ fN. At higher driving force ($F = 300$ fN and $F = 400$ fN), average heat flux increases with increasing substrate temperature. At $F = 300$ fN, the average heat fluxes at $T_W = 190$ K and $T_W = 200$ K increased by 2.5 and 11 times that at $T_W = 180$ K, respectively. At $F = 400$ fN, the average heat fluxes at $T_W = 190$ K and $T_W = 200$ K increased by 0.28 and 232.5 times that at $T_W =$

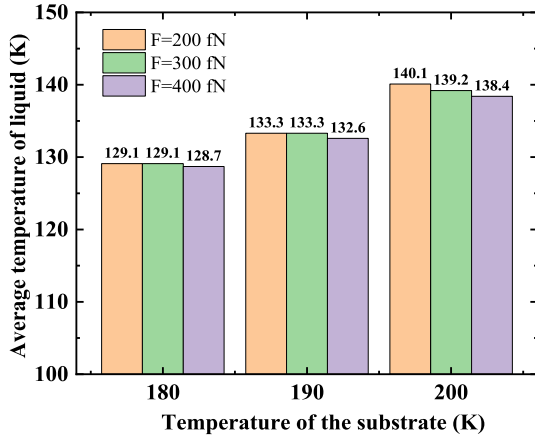


Fig. 11. Variation of the average liquid temperature in the nucleation region during 1000 ps ~ 2000 ps.

180 K, respectively. At $T_W = 200$ K and $F = 200$ fN, the average heat flux density is lower due to the occurrence of film boiling and the deterioration of heat transfer due to the vapor film covering the substrate surface. From the above analysis, it can be seen that substrate temperature has a greater influence on the average heat flux than the driving force.

4. Conclusions

We conducted a systematic investigation of flow boiling of liquid argon on copper surfaces using molecular dynamics methods. The variations of parameters such as fluid flow velocity, onset of boiling time and height of the liquid center of mass are investigated for several working conditions at substrate temperatures of 180 K, 190 K and 200 K and driving forces from 200 fN to 400 fN. The mechanism of enhanced

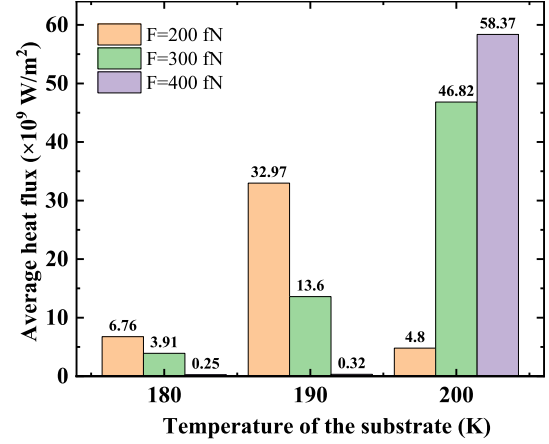


Fig. 13. Variation of average heat flux with time during 2000 ps ~ 4000 ps.

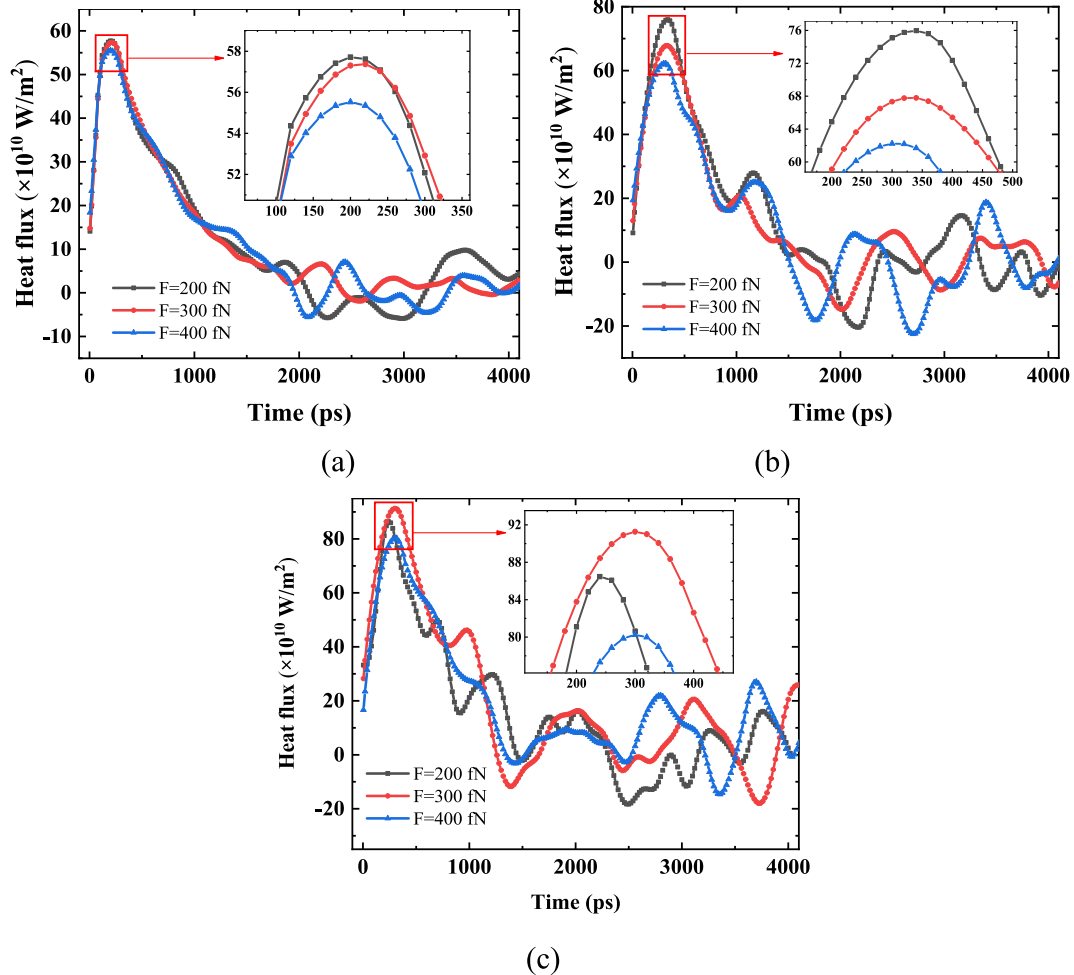


Fig. 12. Variation of heat flux with time for different driving forces (a) $T_W = 180$ K, (b) $T_W = 190$ K, (c) $T_W = 200$ K.

heat transfer was analyzed by the cumulative energy changes of heat source and liquid argon temperature, and the following conclusions were obtained:

- (1) There is a significant velocity gradient in the liquid at the height direction due to the strong interaction force between the liquid and the solid wall, and it increases with the driving force. The overall flow velocity is within the range of 0 m/s ~ 20 m/s and the average flow velocity increases with increasing driving force at the same temperature.
- (2) At substrate temperatures of 180 K and 190 K, the vapor phase always exists in the form of a single bubble or no boiling occurs, and the initial stage of boiling is strongly influenced by the driving force, and the boiling onset time increases with the increasing driving force. When the wall temperature reaches 200 K, boiling is able to respond more quickly due to a sharp increase in the heat transfer capacity from the wall to the fluid. Consequently, at higher temperatures, the boiling onset time is more dependent on the heating temperature than the driving force. After a period of heating at a smaller driving force, the vapor phase will form a vapor film covering the surface of the solid, i.e., film boiling will occur.
- (3) Analyzing the heat transfer efficiency from the heat flux point of view, the maximum heat flux occurs at the initial moment of the third stage when the substrate temperatures are 180 K, 190 K and 200 K. At lower temperatures ($T_W = 180$ K and $T_W = 190$ K), the average heat flux decreases with increasing driving force. At higher temperatures ($T_W = 200$ K), the average heat flux increases with increasing driving force. For a given driving force, the average heat flux increases with increasing substrate temperature, up to 232.5 times ($F = 400$ fN, $T_W = 200$ K). The average heat flux is more dependent on the substrate temperature than on the driving force.

CRediT authorship contribution statement

Shanshan Miao: Writing – original draft, Visualization, Software, Investigation, Formal analysis, Data curation. **Guodong Xia:** Methodology, Funding acquisition, Supervision. **Ran Li:** Writing – original draft, Writing – review & editing.

Declaration of competing interest

The authors declare the following financial interests/personal relationships which may be considered as potential competing interests:

Guodong Xia reports financial support was provided by National Natural Science Foundation of China. If there are other authors, they declare that they have no known competing financial interests or personal relationships that could have appeared to influence the work reported in this paper.

Data availability

Data will be made available on request.

Acknowledgements

This work was supported by the Beijing Natural Science Foundation (No.3242014).

References

- [1] S.J. Hong, X.R. Zheng, C.W. Park, Enhanced flow boiling heat transfer characteristics of R134a on graphene-Cu nanocomposite coating on copper substrate[J], Int. Commun. Heat Mass Transf. 108 (2019) 104343, <https://doi.org/10.1016/j.icheatmasstransfer.2019.104343>.
- [2] S. Wang, H.H. Chen, C.L. Chen, Enhanced flow boiling in silicon nanowire-coated manifold microchannels[J], Appl. Therm. Eng. 148 (2019) 1043–1057, <https://doi.org/10.1016/j.applthermaleng.2018.11.125>.
- [3] F.H. Yang, X.M. Dai, Y. Peles, P. Cheng, J. Khan, C. Li, Flow boiling phenomena in a single annular flow regime in microchannels (I): characterization of flow boiling heat transfer[J], Int. J. Heat Mass Transf. 68 (2014) 703–715, <https://doi.org/10.1016/j.ijheatmasstransfer.2013.09.058>.
- [4] V. Khanikar, I. Mudawar, T. Fisher, Effects of carbon nanotube coating on flow boiling in a micro-channel[J], Int. J. Heat Mass Transf. 52 (15) (2009) 3805–3817, <https://doi.org/10.1016/j.ijheatmasstransfer.2009.02.007>.
- [5] H.A. Mohammed, P. Gunnasegaran, N.H. Shuaib, Influence of channel shape on the thermal and hydraulic performance of microchannel heat sink[J], Int. Commun. Heat Mass Transf. 38 (4) (2010) 474–480, <https://doi.org/10.1016/j.icheatmasstransfer.2010.12.031>.
- [6] S.Y. Guan, Z.H. Zhang, R. Wu, X.K. Gu, C.Y. Zhao, Boiling on nano-porous structures: theoretical analysis and molecular dynamics simulations[J], Int. J. Heat Mass Transf. 191 (2022) 122848, <https://doi.org/10.1016/j.IJHEATMASSTRANSFER.2022.122848>.
- [7] M.J. Liao, L.Q. Duan, Dependencies of surface condensation on the wettability and nanostructure size differences[J], Nanomaterials 10 (2020) 1831, <https://doi.org/10.3390/nano10091831>.
- [8] S. Donatas, K. Yoshiaki, S. Masahiko, O. Taku, Molecular dynamics investigation of surface roughness scale effect on interfacial thermal conductance at solid-liquid interfaces[J], J. Chem. Phys. 150 (11) (2019) 114705, <https://doi.org/10.1063/1.5081103>.
- [9] I. Milica, D.V. Stevanovic, M. Sanja, M.M. Petrovic, New insights into physics of explosive water boiling derived from molecular dynamics simulations[J], Int. J. Heat Mass Transf. 172 (2021) 121141, <https://doi.org/10.1016/J.IJHEATMASSTRANSFER.2021.121141>.
- [10] W.R. Wang, S.H. Huang, X.S. Luo, MD simulation on nano-scale heat transfer mechanism of sub-cooled boiling on nano-structured surface[J], Int. J. Heat Mass Transf. 100 (2016) 276–286, <https://doi.org/10.1016/j.ijheatmasstransfer.2016.04.018>.
- [11] H. Zhao, L.P. Zhou, X.Z. Du, Bubble nucleation on grooved surfaces with hybrid wettability: molecular dynamics study under a transient temperature boundary condition[J], Int. J. Heat Mass Transf. 166 (2021) 120752, <https://doi.org/10.1016/j.ijheatmasstransfer.2020.120752>.
- [12] W. Deng, A. Shakeel, H.Q. Liu, J.T. Chen, J.Y. Zhao, Improving boiling heat transfer with hydrophilic/hydrophobic patterned flat surface: a molecular dynamics study[J], Int. J. Heat Mass Transf. 182 (2022) 121974, <https://doi.org/10.1016/J.IJHEATMASSTRANSFER.2021.121974>.
- [13] W.B. Zhou, D.M. Han, H.L. Ma, Y.K. Hu, G.D. Xia, Microscopic mechanisms behind nucleate boiling heat transfer enhancement on large-aspect-ratio concave nanostructured surfaces for two-phase thermal management[J], Int. J. Heat Mass Transf. 195 (2022) 123136, <https://doi.org/10.1016/J.IJHEATMASSTRANSFER.2022.123136>.
- [14] X.L. Wang, L. Liu, C. Yang, X.Y. Dong, X.M. Yang, Molecular dynamics simulation of liquid film boiling on solid metal and liquid metal surfaces[J], Int. J. Heat Mass Transf. 200 (2023) 123568, <https://doi.org/10.1016/J.IJHEATMASSTRANSFER.2022.123568>.
- [15] D.C. Marable, S. Shin, A.Y. Nobakht, Investigation into the microscopic mechanisms influencing convective heat transfer of water flow in graphene nanochannels[J], Int. J. Heat Mass Transf. 109 (2017) 28–39, <https://doi.org/10.1016/j.ijheatmasstransfer.2017.01.100>.
- [16] P. Chakraborty, T.F. Ma, L. Cao, Y. Wang, Significantly enhanced convective heat transfer through surface modification in nanochannels[J], Int. J. Heat Mass Transf. 136 (2019) 702–708, <https://doi.org/10.1016/j.ijheatmasstransfer.2019.03.053>.
- [17] S.T. Yao, J.S. Wang, X.L. Liu, The impacting mechanism of surface properties on flow and heat transfer features in nanochannel[J], Int. J. Heat Mass Transf. 176 (2021) 121441, <https://doi.org/10.1016/J.IJHEATMASSTRANSFER.2021.121441>.
- [18] S.T. Yao, J.S. Wang, X.L. Liu, Role of wall-fluid interaction and rough morphology in heat and momentum exchange in nanochannel[J], Appl. Energy 298 (2021) 117183, <https://doi.org/10.1016/J.APENERGY.2021.117183>.
- [19] M. Amirhosein, Z. Majid, T. Davood, R. Amin, K. Aliakbar, Boiling of Argon flow in a microchannel by considering the spherical geometry for roughness barriers using molecular dynamics simulation[J], J. Mol. Liq. 321 (2020) 114462, <https://doi.org/10.1016/j.molliq.2020.114462>.
- [20] Y. Xu, X.Y. Zhang, S. Allahyari, A. Alizadeh, D. Toghraie, A. Rahmani, The effects of shape of barriers on normal distribution of fluid within different regions of microchannels using molecular dynamics simulation[J], J. Mol. Liq. 338 (2021) 116672, <https://doi.org/10.1016/j.molliq.2021.116672>.
- [21] S. Rostami, M. Zarringhalam, A. Alizadeh, D. Toghraie, A.S. Gordanlou, Molecular dynamic simulation of Argon boiling flow inside smooth and rough microchannels by considering the effects of cubic barriers[J], J. Mol. Liq. 312 (2020) 113130, <https://doi.org/10.1016/j.molliq.2020.113130>.
- [22] X.Y. Yin, C.Z. Hu, M.L. Bai, J.Z. Lv, An investigation on the heat transfer characteristics of nanofluids in flow boiling by molecular dynamics simulations[J], Int. J. Heat Mass Transf. 162 (2020) 120338, <https://doi.org/10.1016/j.ijheatmasstransfer.2020.120338>.
- [23] X.Y. Yin, M.L. Bai, C.Z. Hu, J.Z. Lv, Molecular dynamics simulation on the effect of nanoparticle deposition and nondeposition on the nanofluid explosive boiling heat transfer[J], Numer. Heat Transf. A Appl. 73 (8) (2018) 553–564, <https://doi.org/10.1080/10407782.2018.1459135>.
- [24] R.L. Rishi, P. Jayaramu, S. Gedupudi, S.K. Das, Experimental investigation of the influence of boiling-induced ageing on high heat flux flow boiling in a copper

- microchannel[J], *Int. J. Heat Mass Transf.* 181 (2021) 121862, <https://doi.org/10.1016/j.ijheatmasstransfer.2021.121862>.
- [25] B.R. Fu, C.Y. Lee, C. Pan, The effect of aspect ratio on flow boiling heat transfer of HFE-7100 in a microchannel heat sink[J], *Int. J. Heat Mass Transf.* 58 (1–2) (2013) 53–61, <https://doi.org/10.1016/j.ijheatmasstransfer.2012.11.050>.
- [26] G. Nagayama, P. Cheng, Effects of interface wettability on microscale flow by molecular dynamics simulation[J], *Int. J. Heat Mass Transf.* 47 (2004) 501–513, <https://doi.org/10.1016/j.ijheatmasstransfer.2003.07.013>.
- [27] S.S. Miao, G.D. Xia, Molecular dynamics investigation of the effect of nanostructured surfaces on flow boiling[J], *J. Mol. Liq.* 400 (2024) 124457, <https://doi.org/10.1016/j.molliq.2024.124457>.
- [28] F. Moučka, I. Nezbeda, W.R. Smith, Molecular force field development for aqueous electrolytes: 1. Incorporating appropriate experimental data and the inadequacy of simple electrolyte force fields based on Lennard-Jones and point charge interactions with Lorentz-Berthelot rules[J], *J. Chem. Theory Comput.* 9 (11) (2013) 5076–5085, <https://doi.org/10.1021/ct4006008>.
- [29] A. Stukowski, Visualization and analysis of atomistic simulation data with OVITO—the Open Visualization Tool[J], *Model. Simul. Mater. Sci. Eng.* 18 (1) (2010) 015012, <https://doi.org/10.1088/0965-0393/18/1/015012>.
- [30] P. Bai, L.P. Zhou, X.Z. Du, Effects of liquid film thickness and surface roughness ratio on rapid boiling of water over copper plates[J], *Int. Commun. Heat Mass Transf.* 120 (2020) 105036, <https://doi.org/10.1016/j.icheatmasstransfer.2020.105036>.
- [31] L.Y. Zhang, J.L. Xu, G.L. Liu, J.P. Lei, Nucleate boiling on nanostructured surfaces using molecular dynamics simulations[J], *Int. J. Therm. Sci.* 152 (2020) 106325, <https://doi.org/10.1016/j.ijthermalsci.2020.106325>.
- [32] Y. Li, W.J. Zhou, Y.H. Zhang, B.J. Qi, J.J. Wei, A molecular dynamics study of surface wettability effects on heterogeneous bubble nucleation[J], *Int. Commun. Heat Mass Transf.* 119 (2020) 104991, <https://doi.org/10.1016/j.icheatmasstransfer.2020.104991>.